Nuclear Inst. and Methods in Physics Research, A 910 (2018) 90–95

Contents lists available at ScienceDirect

Nuclear Inst. and Methods in Physics Research, A

journal homepage: www.elsevier.com/locate/nima

Monte-Carlo based performance assessment of ASACUSA's antihydrogen detector

Y. Nagata [a,b,*], N. Kuroda [c], B. Kolbinger [d], M. Fleck [d,1], C. Malbrunot [d,e], V. Mäckel [d,2], C. Sauerzopf [d,3], M.C. Simon [d], M. Tajima [c,4], J. Zmeskal [d], H. Breuker [e], H. Higaki [f], Y. Kanai [g], Y. Matsuda [c], S. Ulmer [b], L. Venturelli [h,i], E. Widmann [d], Y. Yamazaki [b]

[a] Department of Physics, Tokyo University of Science, 1-3 Kagurazaka, Shinjuku, 162-8601 Tokyo, Japan
[b] Ulmer Fundamental Symmetries Laboratory, RIKEN, 2-1 Hirosawa, Wako-shi, 351-0198 Saitama, Japan
[c] Institute of Physics, University of Tokyo, 3-8-1 Komaba, Meguro-ku, 153-8902 Tokyo, Japan
[d] Stefan-Meyer-Institut für Subatomare Physik, Österreichische Akademie der Wissenschaften, Wien 1090, Austria
[e] CERN, Genève 1211, Switzerland
[f] Graduate School of Advanced Sciences of Matter, Hiroshima University, 739-8530 Hiroshima, Japan
[g] RIKEN Nishina Center for Accelerator-Based Science, 2-1 Hirosawa, Wako-shi, 351-0198 Saitama, Japan
[h] Dipartimento di Ingegneria dell'Informazione, Università di Brescia, Brescia 25133, Italy
[i] Istituto Nazionale di Fisica Nucleare, Sez. di Pavia, I-27100 Pavia, Italy

ARTICLE INFO

Keywords:
Antihydrogen
Antimatter
Detector
Calorimeter
Tracker

ABSTRACT

An antihydrogen detector consisting of a thin BGO disk and a surrounding plastic scintillator hodoscope has been developed. We have characterized the two-dimensional positions sensitivity of the thin BGO disk and energy deposition into the BGO was calibrated using cosmic rays by comparing experimental data with Monte-Carlo simulations. The particle tracks were defined by connecting BGO hit positions and hits on the surrounding hodoscope scintillator bars. The event rate was investigated as a function of the angles between the tracks and the energy deposition in the BGO for simulated antiproton events, and for measured and simulated cosmic ray events. Identification of the antihydrogen Monte Carlo events was performed using the energy deposited in the BGO and the particle tracks. The cosmic ray background was limited to 12 mHz with a detection efficiency of 81%. The signal-to-noise ratio was improved from 0.22 $s^{-1/2}$ obtained with the detector in 2012 to 0.26 $s^{-1/2}$ in this work.

1. Introduction

Recently, antihydrogen ($\bar{H}$) atoms have been produced [1] in a unique cusp trap [2–4] developed for the in-flight hyperfine spectroscopy of ground state $\bar{H}$ atoms [5–7]. The most recent progress is reported in [8–10]. In 2012, the ASACUSA Cusp collaboration developed a $\bar{H}$ detector consisting of a BGO ($Bi_4Ge_3O_{12}$) scintillator disk in combination with a single anode photomultiplier (PMT) and 5 plastic scintillator plates. The detector was able to reject cosmic backgrounds with a high efficiency [11]. In order to further improve the background rejection efficiency, we have developed a new $\bar{H}$ detector. The single anode PMT has been replaced by 4 multi-anode PMTs (MAPMTs) for 2D photon readout of the BGO. The five plastic scintillators were replaced by a two-layer hodoscope with 32 plastic scintillator bars per layer to determine charged particle tracks with higher resolution [12].

2. $\bar{H}$ detector

Fig. 1 shows a schematic diagram of the structure of the new $\bar{H}$ detector consisting of the thin BGO disk and the hodoscope. The BGO disk, has a diameter of 90 mm and a thickness of 5 mm and is housed on the vacuum side (10^{-7} Pa) of a UHV viewport. The front surface of the BGO disk was coated with a carbon layer of thickness 0.7 μm to reduce multireflections of the light from scintillation on the surface. It was found that the carbon coating improved the position resolution by a factor of ~2 in our previous device [13]. To achieve a position sensitive readout, 4 MAPMTs (Hamamatsu H8500C) each having 8 × 8 anodes with effective area of 49 mm × 49 mm were directly placed on the view port glass as shown in Fig. 2. The output of 8 × 8 anodes were amplified, digitized and stored by an amplifier unit (Clear Pulse 80190) which was

* Corresponding author at: Department of Physics, Tokyo University of Science, 1-3 Kagurazaka, Shinjuku, 162-8601 Tokyo, Japan.
E-mail address: yugo.nagata@rs.tus.ac.jp (Y. Nagata).
[1] Present address: Institute of Physics, University of Tokyo, 3-8-1 Komaba, Meguro-ku, 153-8902, Tokyo, Japan.
[2] Present address: Ulmer Fundamental Symmetries Laboratory, RIKEN, 2-1 Hirosawa, Wako-shi, 351-0198, Saitama, Japan.
[3] Present address: Data Technology, Vienna, Austria.
[4] Present address: RIKEN Nishina Center for Accelerator-Based Science, 2-1 Hirosawa, Wako-shi, 351-0198, Saitama, Japan.

https://doi.org/10.1016/j.nima.2018.09.013
Received 11 June 2018; Received in revised form 4 September 2018; Accepted 4 September 2018
Available online xxxx

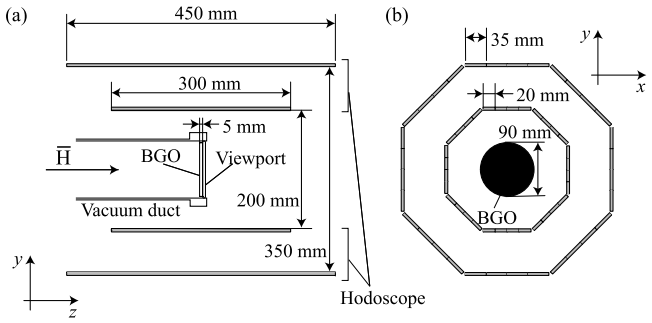

Fig. 1. Cross section of the H̄ detector along the beam axis (a) and perpendicular to the H̄ beam axis (b).

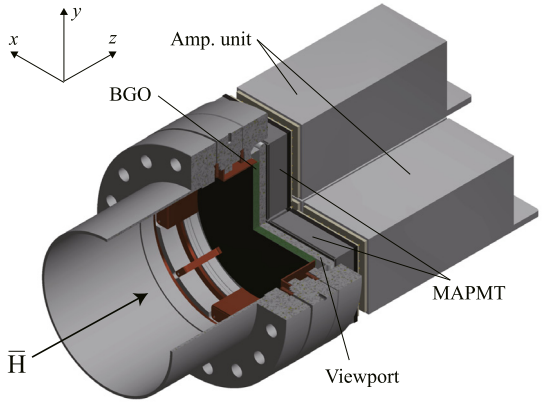

Fig. 2. Three quarter section view of the 2D sensitive BGO detector.

a dedicated model for the H8500C and included 8 × 8 charge amplifiers and analogue-to-digital converters with 12 bit resolution.

The hodoscope consists of two layers of 32 plastic scintillator bars arranged in an octagonal configuration [12]. The scintillator bars are 300 mm × 20 mm × 5 mm for the inner layer and 450 mm × 35 mm × 5 mm for the outer. With face to face distances of 200 mm and 350 mm respectively for the inner and outer layers (see Fig. 1(a)). The solid angle covered by the scintillator bars in units of 4π seen from the center of the BGO is $\omega \sim 80\%$. Silicon photomultipliers (SiPM, KETEK PM3350TS) were connected to both ends of each bar. The output pulses from the SiPMs was amplified by dedicated front end modules described in detail elsewhere (see Ref. [14]) and recorded by 128 channels waveform digitizers (CAEN V1742).

Meshes to which a high voltage can be applied is installed at the upstream of the detector to reject the antiprotons leaking from the cusp trap for the measurement of the H̄ atoms [15].

3. 2D distribution of cosmic rays

To obtain the relative sensitivity of each channel, 4 MAPMTs were assembled and irradiated by pulsed (200 ns width) light from a LED with the peak wavelength of 470 nm (see also Ref. [13]), the peak emission wavelength of the BGO scintillation light was 480 nm. The voltages applied to the MAPMTs were adjusted such that the total output charge of each MAPMT were equal.

Fig. 3(a) shows an example of a 2D map of output charges from one of the 4 MAPMTs averaged over 10^4 pulses of LED light. The channel with the maximum output charge is arbitrarily set to 100 and all other channels are scaled accordingly. The relative gain of the channels of each MAPMT are evaluated using this mapping. This result was compared with the data sheet from the manufacturer where a tungsten filament lamp was used for calibration. By taking the ratio between

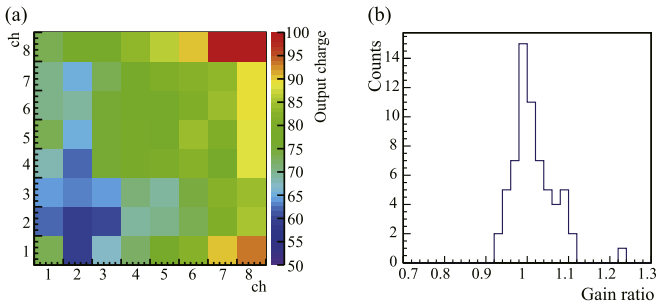

Fig. 3. (a) Example of a 2D map of averaged output charges of one of the 4 MAPMTs investigated by LED light. (b) Distribution of the gain ratio between the measured values and the data sheet values for each channel.

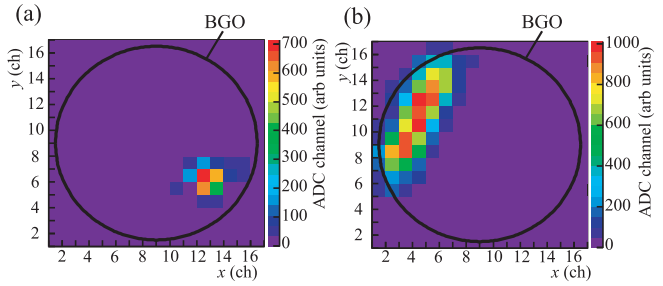

Fig. 4. Examples of 2D charge distributions of cosmic rays events where the BGO surface has been penetrated nearly perpendicularly (a) or at grazing incidence (b).

the measured values and those from the data sheet for each anode, the distribution of the gain ratio as shown in Fig. 3(b) was obtained. The standard deviation of this distribution is around 5%.

Fig. 4(a) and (b) show the 2D charge distribution for two example cosmic rays events after offline gain matching of the individual MAPMT channels described above. In these examples, the BGO surface has been penetrated nearly perpendicularly (a) or at grazing incidence (b). These figures demonstrate that position sensitive readout has been successfully implemented using 2D MAPMTs.

In order to reconstruct particle tracks (to be discussed in detail later), we define the position of a hit on the BGO as the center of the anode giving the highest output charge. When the hit positions observed in the 2D distribution are outside of the BGO, such events are removed in the analysis because they are probably Čerenkov light generated in the optics of the MAPMT or the viewport when high energy charged particles pass through them. The total charge Q is obtained by summing the charges from all channels (see Fig. 4(a) and (b)).

4. Energy calibration of the BGO detector

For the energy calibration, cosmic rays were measured and the charge distribution $f(Q)$ was compared with the energy deposition distribution $g(E)$ calculated by a Monte-Carlo simulation using the Geant4 toolkit[5] [16]. Blue solid circles in Fig. 5 show $f(Q)$ for cosmic rays events when more than 2 inner hodoscope bars are hit in any coincident combination. A bar is considered to be 'hit' when there is a coincidence between the signals of the upstream and downstream SiPMs connected to the bar.

The simulation includes the BGO detector together with the viewport and the vacuum duct (see Fig. 1(a)). Cosmic rays are generated by the CRY package [17]; Čerenkov light however is not included. $g(E)$

[5] Geant4.9.6 Patch-02 was used.

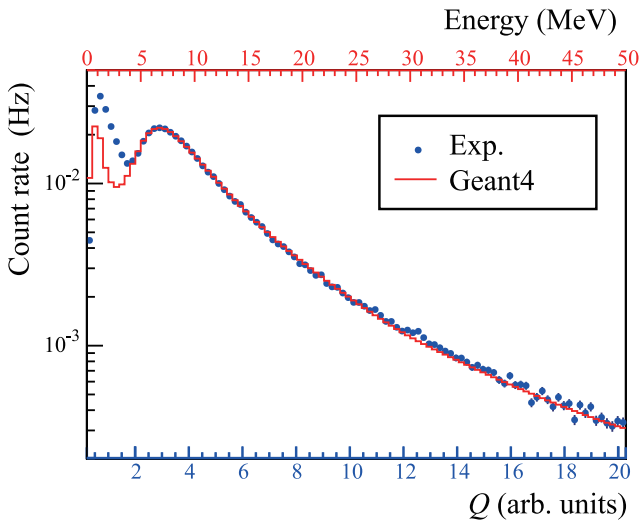

Fig. 5. The blue solid circles show the total measured output charge of cosmic ray events. The red line shows the simulated energy deposition distributions. The integral of events with $E \geq 50$ MeV was 3% of those with $E \geq 4.5$ MeV.

is convoluted with the energy resolution which is assumed to be proportional to $\sqrt{E}$ [18], i.e.,

$$G(E) = \int g(E') \frac{1}{\sqrt{2\pi(\alpha\sqrt{E'})^2}} e^{-(E-E')^2/2(\alpha\sqrt{E'})^2} dE',$$

where α is a fitting parameter. To compare $f(Q)$ and $G(E)$, the relation $E = \eta Q + E_c$ is assumed, where η and E_c are fitting parameters. E_c corresponds to the contribution of Čerenkov light generated in the BGO and the glass. $G(E)$ is fit to $f(Q)$ using least squares method in the energy range from 4.5 to 50 MeV with 3 free parameters α, η and E_c. The result is shown by the red line in Fig. 5. The goodness of the fit is given by $\chi^2/\text{ndf} = 1.65$ for $\alpha = 0.52$ $\sqrt{\text{MeV}}$, $\eta = 2.5$ in units proportional to charge over energy and $E_c = 0.50$ MeV. The discrepancy between the experiment and the simulation at $E < 4$ MeV would be caused by Čerenkov light. The fitting parameter E_c was introduced to compensate this discrepancy.

The cosmic ray flux distribution is known to follow $\cos^2\theta_z$, where θ_z is the zenith angle. In this case, the average path length of cosmic rays in the BGO is evaluated to be approximately 8 mm. Considering that the energy deposited by a minimum ionizing particle (MIP) in the BGO is 9.0 MeV/cm [19], the peak at around 7 MeV in Fig. 5 is attributed to MIPs. As explained below (see Section 5.3), only events for $E > E_{th} = 15$ MeV are considered in the following sections.

5. Identification of $\bar{H}$ atoms and cosmic ray suppression

Fig. 6 shows a simplified back view of the $\bar{H}$ detector where the signals from the 4 MAPMTs (shown in the square in the center) and the hodoscope bars (the outermost octagonal arrangement) for a typical cosmic event in the experiment are overlaid.

In this example, a spot like pattern is seen on the BGO. Green-colored hodoscope bars are simultaneously hit by the cosmic ray. The red shaded area in the upper left side shows the possible spatial range of the trajectory of the charged particle.

As a best guess, the bisector of the shaded area is taken to define a track which is shown by the thick black line. In the lower right side, 2 neighboring hodoscope bars are hit, in this case, the red shaded area is defined from the edges of the neighboring hodoscope bars and the BGO hit position. The particle track is also defined by a bisector of the shaded area. In this example, the number of tracks is $k = 2$.

Solid and dashed lines in Fig. 7 show the experimental and simulated results of cosmic ray count rate n_k^c as a function of k. The highest n_k^c is

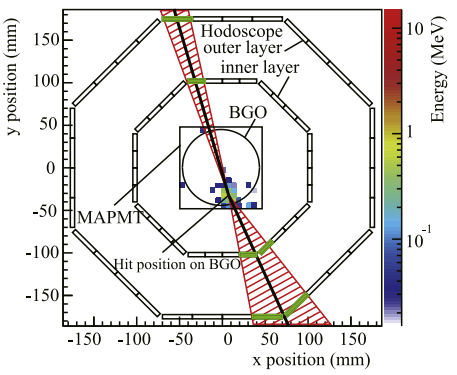

Fig. 6. Example of a cosmic ray event with $k = 2$ tracks. The circle and surrounding square in the center show the BGO disk and the total area covered by the 4 MAPMTs, respectively. The external octagonal configurations show the inner and outer hodoscope layers. (For interpretation of the references to color in this figure legend, the reader is referred to the web version of this article.)

observed for $k = 2$ and decreases by more than one order of magnitude for each additional unit of k. The track number analysis for simulations of antiprotons ($\bar{p}$) irradiating the BGO disk uniformly with the typical count rate of the $\bar{H}$ atoms in the experiment $I_{\bar{p}} = 0.1$ Hz results in the dash–dot (green online) curve ($n_k^{\bar{p}}$).

In this simulation, the CHIPS model was used in Geant4 for $\bar{p}$ annihilation. This model was previously tested with respect to the energy deposition analysis for $\bar{H}$ annihilation in the BGO [1,11]. The multiplicity of annihilation products from $\bar{p}$ annihilation was studied using an emulsion detector and agreed with CHIPS results except for annihilation with heavy atoms[6] [20].

Also the $n_k^{\bar{p}}$ curve has a maximum at $k = 2$, although its evolution is much less dependent on k than n_k^c. When a $\bar{p}$ annihilates with a nucleus, approximately 3 charged and 2 neutral pions are produced on average [21]. Taking into account the charged pions and the solid angle ω covered by the hodoscope, $n_2^{\bar{p}}$ is estimated to be $3\omega^2(1-\omega)I_{\bar{p}} \sim 0.04$ Hz which can be compared to $n_2^{\bar{p}} \sim 0.03$ Hz in Fig. 7.

As will be discussed in Section 5.4, n_k^c can be decreased considerably from the dashed line and is around 5×10^{-3} Hz as shown by the open circles in Fig. 7 for $k = 1$, 2 and 3.

Alternatively, $n_k^{\bar{p}}$ does not decrease very much as seen from the open triangles. In these cases, n_k^c is well below $n_k^{\bar{p}}$. Further to this, n_4^c is more than one order of magnitude lower than the open circles and is negligibly small. Therefore we can assume that events for $k \geq 4$ can be reasonably attributed to $\bar{p}$ annihilation. In the following subsections, the events for $k = 2$, $k = 3$ and then $k = 1$ are considered.

5.1. Events for $k = 2$

To analyze 2-track events, the track direction is defined by the angle measured anticlockwise from a horizontal line on the $x - y$ plane as shown in Fig. 8. The tracks are numbered in ascending ordered with increasing angle. The corresponding angles of the 1st and the 2nd tracks are named θ_1 and θ_2 ($\theta_1 < \theta_2$), respectively. Further we define $\theta_{12} = \theta_2 - \theta_1$.

Fig. 9(a) and (b) compare the 2D distribution of cosmic events as a function of θ_1 and θ_{12} as obtained from experiment and simulation, respectively.

It can be seen that the simulation result reproduces the experimental result well. A strong ridge is observed at $\theta_{12} \sim 180$ degrees which

[6] It is noted that there are no systematic studies of both multiplicity of annihilation products, and their energy deposition for $\bar{p}$ annihilation at rest. To investigate this, fragmentation studies of antiproton–nucleus annihilation are being performed using a Timepix3 detector within the ASACUSA collaboration.

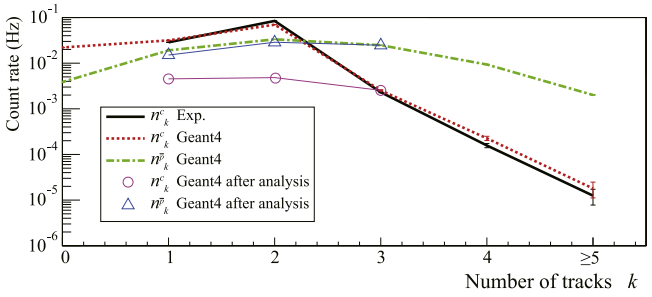

Fig. 7. Solid and dashed lines show experimental and simulated results of cosmic ray count rate n_k^c as a function of k, respectively. The dash–dot curve shows the simulation result of the annihilation count rate $n_k^{\bar{p}}$ when $\bar{p}$s irradiate the BGO disk uniformly with a rate of $I_{\bar{p}} = 0.1$ Hz. Only events depositing more than 15 MeV in the BGO were considered for both cosmic rays and $\bar{p}$s in the simulated and experimental data. The open circles and triangles show the simulated data of n_k^c and $n_k^{\bar{p}}$ for k = 1–3 obtained from the analysis described in the Section 5.4, respectively.

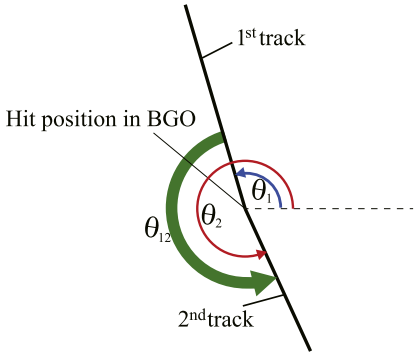

Fig. 8. Definitions of θ_1, θ_2 and θ_{12}.

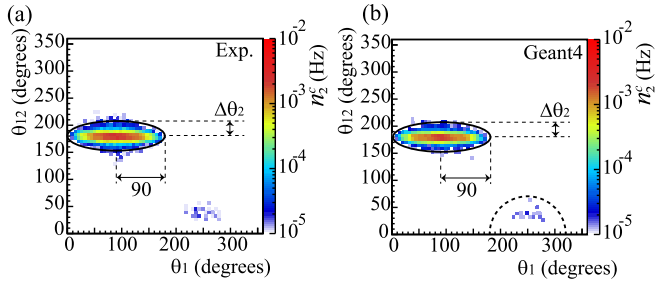

Fig. 9. (a) Experimental result of the 2D distribution of n_2^c as a function of θ_1 and θ_{12}. (b) Simulation result of n_2^c as a function of θ_1 and θ_{12}. In both figures, E_{th} = 15 MeV. The bin widths are 6 degrees on both axes. The ellipse is defined by semi-minor axis $\Delta\theta_2$ and semi-major axis of 90 degrees in θ_{12} and θ_1, respectively, and is used for background suppression.

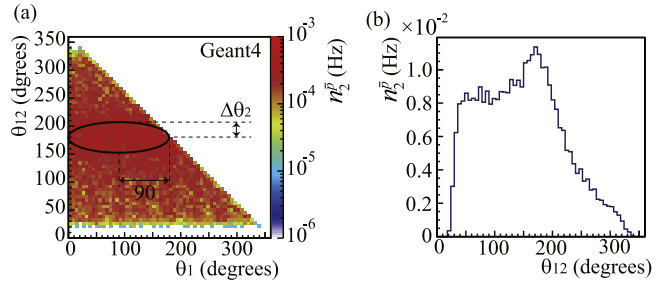

Fig. 10. (a) Experimental result of 2D distribution of $n_2^{\bar{p}}$ as a function of θ_1 and θ_{12} with E_{th} = 15 MeV. The bin widths are 6 degrees on both axes. (b) Projection of (a) onto θ_{12} axis. The ellipse is defined like in Fig. 9.

corresponds to cosmic rays passing straight through the detector. On the other hand, in θ_1 direction, a broad distribution, centered at 90 degrees, reflects the cosmic ray flux following a $\cos\theta_z^2$ distribution.

Fig. 10(a) shows the result of the simulation of the 2D distribution of $n_2^{\bar{p}}$ as a function of θ_1 and θ_{12}. The distribution is very broad, as is expected from $\bar{p}$ annihilations at low energy.

The n_2^c background can be decreased by removing events inside an ellipse defined by semi-minor axis $\Delta\theta_2$ and semi-major axis of 90 degrees in θ_{12} and θ_1, respectively (see Fig. 9). For example, the n_2^c background is reduced by one order of magnitude for $\Delta\theta_2$ = 10 degrees. Using the same cut, only about 10% of the $\bar{p}$s are removed because of the different distributions of Figs. 9 and 10.

It is noted that in both Fig. 9(a) and (b), we observe an additional small peak at $\theta_1 \sim 270$ degrees and $\theta_{12} \sim 40$ degrees. Investigating the corresponding events inside the dotted half circle in Fig. 9(b), the simulation shows that those events are caused by incident cosmic rays of γ rays (~80%), e^+ or e^- (~10%), and μ^+ or μ^- (~10%). Therefore it seems that the main component of this peak is attributed to the γ rays producing e^--e^+ pairs in the BGO. The fraction of these events is 1% of the total events in Fig. 9(a) and (b).

In comparison, although the distribution of $n_2^{\bar{p}}$ in Fig. 10(a) is very broad, it has a peak at $\theta_{12} \sim 180$ degrees as shown in Fig. 10(b) which is the projection of (a) onto the θ_{12} axis.

The preference at 180 degrees can be explained if we consider a specific type of event, one with three charged pions. When two charged pions hit the hodoscope, with the third pion escaping in a direction close to the beam axis, momentum conservation will favor θ_{12} around 180 degrees. These (real) events are of course removed by the elliptical cut introduced to remove cosmic events.

5.2. Events for $k = 3$

The track directions for $k = 3$ are defined in the same manner in the case of $k = 2$. Because 3 tracks are involved, there are 3 ways to choose track pairs, which can then be described in an equivalent manner to 2-track events as shown in Fig. 11(a)–(c).

Fig. 12(a) and (b) show the experimental and simulated results of the 2D distributions of n_3^c, obtained by summing 3 distributions of θ_{12} vs. θ_1, θ_{13} vs. θ_1 and θ_{23} vs. θ_2, i.e. every event is represented by 3 points corresponding to Fig. 11(a)–(c) on the plot to conveniently summarize them. The simulation reproduces the experiment very well.

A peak at $\theta_{ij} \sim 180$ degrees is observed, which is broader than the peak in Fig. 9(a) and (b). By investigating the corresponding events in the simulation, it was found that a cosmic ray from above generates recoil electrons emitted downward in the BGO which forms the broad peak (see Fig. 11(a) and (b)). Another peak is seen at $\theta_i \sim 270$ degrees which is formed by the recoil electron together with the incident cosmic ray (see Fig. 11(c)).

Fig. 13 shows the simulation result of $n_3^{\bar{p}}$ as per Fig. 12(a) and (b) for n_3^c. The distribution is more evenly populated than $k = 2$.

Equivalently to the case of $k = 2$, the cosmic ray events are expected to be reduced by removing events inside the ellipse (see Fig. 12) defined by semi-minor axis $\Delta\theta_3$ and semi-major axis of 90 degrees in θ_{ij} and θ_i, respectively. Whilst simultaneously not decreasing $n_3^{\bar{p}}$ very much. It is noted that the peak at $\theta_i \sim 270$ degrees in Fig. 12(a) and (b) is not present when the events inside the ellipse are removed, because the events of $\theta_i \sim 270$ degrees (see also Fig. 11(c)) are the reflection of the events of $\theta_{ij} \sim 180$ degrees (see also Fig. 11(a) and (b)).

5.3. Signal-to-noise ratio (SNR) for $k \geq 2$

The total rate of cosmic events after the data cut was obtained by taking the sum of n_k^c for k and is defined by $N_i^c = \Sigma_{k \geq i} n_k^c$. Fig. 14(a) and (b) show the experimental and simulated results of the 2D distributions of N_2^c, respectively, as a function of $\Delta\theta_2$ and $\Delta\theta_3$.

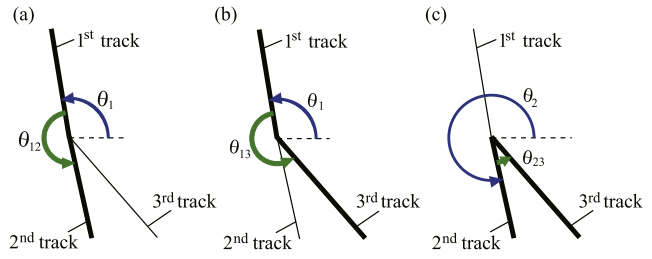

Fig. 11. Combinations of 2 out of 3 tracks. Angles θ_1, θ_2, θ_{12}, θ_{13} and θ_{23} are defined.

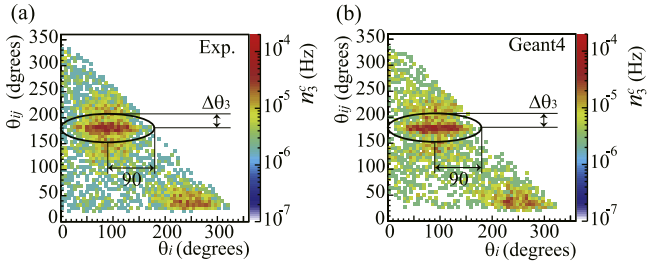

Fig. 12. (a) Experimental results of n_3^c obtained by summing 3 distributions of θ_{12} vs. θ_1, θ_{13} vs. θ_1 and θ_{23} vs. θ_2. (b) Simulation result of the same distributions as in (a). In both figures, E_{th} = 15 MeV. The bin widths are 6 degrees on both axes. The ellipse is defined by semi-minor axis $\Delta\theta_3$ and semi-major axis of 90 degrees in θ_{ij} and θ_i, respectively, and is used for background suppression.

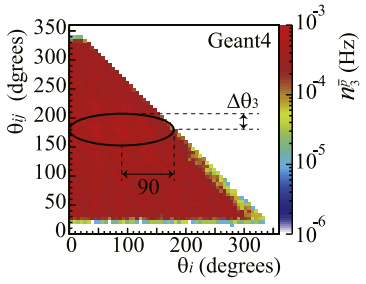

Fig. 13. Result from simulations of $n_3^{\bar{p}}$ obtained by summing 3 distributions of θ_{12} vs. θ_1, θ_{13} vs. θ_1 and θ_{23} vs. θ_2 with E_{th} = 15 MeV. The bin widths are 6 degrees on both axes. The ellipse is defined as in Fig. 12.

The simulations reproduce the experimental data well. To evaluate the difference between the data and the simulation quantitatively, Fig. 14(c) and (d) show experimental and simulated results of N_2^c as a function of $\Delta\theta_2$ for $\Delta\theta_3$ = 0, 30, 60 and 90 degrees. The difference between the experimental and simulated results is less than 10%. In the later discussion, we analyze the simulation data.

Fig. 15(a) shows the simulation result of the detection efficiency ϵ_2 of $\bar{p}$'s defined by $\epsilon_i = N_i^{\bar{p}}/I_{\bar{p}}$ as a function of $\Delta\theta_2$ and $\Delta\theta_3$, where $N_i^{\bar{p}} = \Sigma_{k\geq i} n_k^{\bar{p}}$. It is shown that ϵ_2 decreases as $\Delta\theta_2$ and $\Delta\theta_3$ increase. We define the signal-to-noise ratio (SNR) by $x_i = \frac{N_i^{\bar{p}}}{\sqrt{N_i^{\bar{p}}+N_i^c}}$. Fig. 15(b) shows the 2D distribution of x_2 as a function of $\Delta\theta_2$ and $\Delta\theta_3$. The maximum x_2 is 0.24 $s^{-1/2}$ at $\Delta\theta_2$ = 16 degrees and $\Delta\theta_3$ = 0 degrees with N_2^c = 6.9 mHz and ϵ_2 = 65%. As is seen in Fig. 15(b), to maximize x_2, $\Delta\theta_3$ should be 0 for all values $\Delta\theta_2$. This suggests that all events of $n_3^{\bar{p}}$ can be identified as $\bar{p}$s. It is noted that this fact and the optimization of the SNR depend on $I_{\bar{p}}$.

Fig. 16 shows x_2 as a function of E_{th}, x_2 has a maximum at E_{th} = 15 MeV, but varying only within 1% in the range of 5 MeV < E_{th} < 20 MeV. Therefore E_{th} is not critical to the optimization of x_2 in this range.

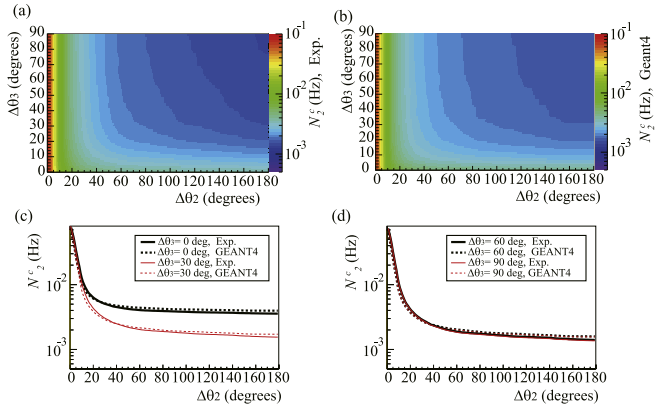

Fig. 14. (a) Experimental result of the 2D distribution of N_2^c as a function of $\Delta\theta_2$ and $\Delta\theta_3$. (b) Corresponding simulation result for N_2^c. The bin widths in Figs. (a) and (b) are 1 degree on both axes. (c) and (d) Experimental and simulated results of N_2^c as a function of $\Delta\theta_2$ for $\Delta\theta_3$ = 0, 30, 60 and 90 degrees. In these figures, E_{th} = 15 MeV.

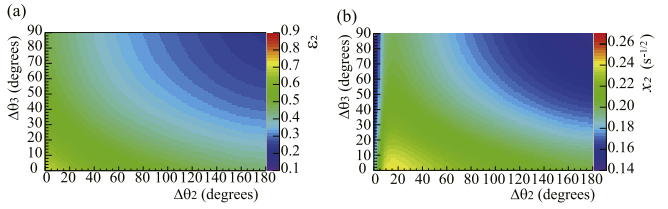

Fig. 15. (a) The simulation result of 2D distribution of ϵ_2 as a function of $\Delta\theta_2$ and $\Delta\theta_3$. (b) The simulation result of x_2 as a function of $\Delta\theta_2$ and $\Delta\theta_3$. In these figures, E_{th} = 15 MeV. The bin widths are 1 degree on both axes.

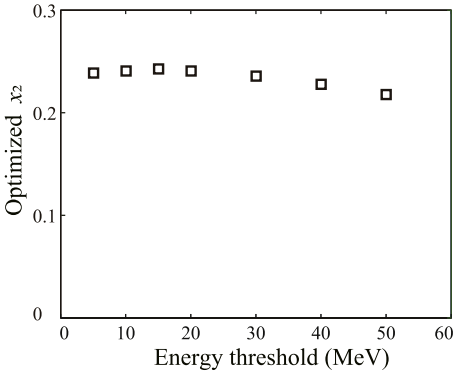

Fig. 16. x_2 as a function of E_{th}, where x_2 is optimized for each E_{th} using the procedure described in Section 5.3.

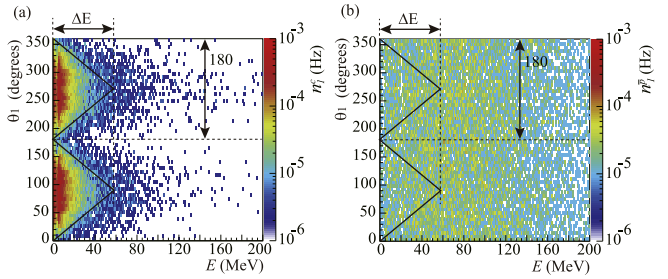

Fig. 17. (a) Simulation result of the 2D distribution of n_1^c as a function of E and θ_1. (b) Simulation result of the 2D distribution of $n_1^{\bar{p}}$ as a function of E and θ_1. The bin widths in horizontal and vertical axes are 1 MeV and 6 degrees, respectively.

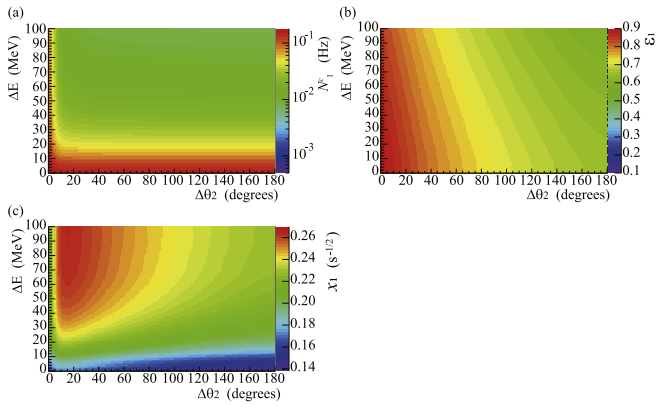

Fig. 18. (a) Simulation result of 2D distributions of N_1^c as a function of $\Delta\theta_2$ and ΔE. (b) ϵ_1 as a function of $\Delta\theta_2$ and ΔE. (c) x_1 as a function of $\Delta\theta_2$ and ΔE. In these figures, E_{th} for $k \geq 2$ is 15 MeV. The bin widths are 1 degree on both axes.

5.4. Events for $k = 1$ and SNR

Fig. 17(a) shows the 2D distribution of n_1^c as a function of the energy E deposited in the BGO and of θ_1. We observe a ridge at $E \sim 7$ MeV which corresponds to the MIP peak. In the θ_1 direction, the broad distribution has two maxima, at 90 and at 270 degrees; its shape can be attributed to the cosmic ray flux distribution of $\cos\theta_z^2$. The shape of the ridge appears to be an ellipse. However, the tail of the ridge seems to follow a more triangular shape. Fig. 17(b) shows the 2D distribution of $n_1^{\bar{p}}$ as a function of E and θ_1. The distribution is very broad. Background from n_1^c is expected to be reduced by removing events inside the triangular regions defined in Fig. 17(a) and (b).

Fig. 18(a) and (b) show the 2D distributions of N_1^c and ϵ_1 ($k \geq 1$), respectively, as a function of $\Delta\theta_2$ and ΔE. It is seen that N_1^c and ϵ_1 decrease gradually as $\Delta\theta_2$ and ΔE increase. Fig. 18(c) shows x_1 as a function of $\Delta\theta_2$ and ΔE. The maximum of x_1 of 0.26 s$^{-1/2}$ is reached at $\Delta\theta_2 = 14$ degrees and $\Delta E = 93$ MeV with $N_1^c = 12$ mHz and $\epsilon_1 = 81\%$. This is larger than the maximum value of x_2, therefore, the analysis including the events for $k = 1$ improves the SNR. Comparing with the $\bar{\text{H}}$ detector developed in 2012 with $x = 0.22$ s$^{-1/2}$ with the cosmic count rate of 4 mHz and a detection efficiency of 50% for $I_{\bar{p}} = 0.1$ Hz, the detector described in this work improves upon the SNR and the detection efficiency.

6. Conclusion

We have developed a $\bar{\text{H}}$ detector consisting of a thin BGO disk and a hodoscope. We have measured hit positions of cosmic rays in the BGO disk and confirmed that the thin disk with a 2D readout by MAPMTs enables position sensitivity. The energy deposition in the BGO was calibrated by comparing cosmic ray data with Geant4 simulations. Charged particle tracks were determined by connecting the hit position on the BGO and hits on hodoscope bars. By removing the cosmic rays passing through the detector using the cut on ΔE, $\Delta\theta_2$ and E_{th}, the background was reduced efficiently to $N_1^c = 12$ mHz with a detection efficiency of $\epsilon_1 = 81\%$. The SNR was improved to $x_1 = 0.26$ s$^{-1/2}$ which was compared to 0.22 s$^{-1/2}$ for the detector used in 2012.

Acknowledgments

We would like to thank Tomohiro Kobayashi for the carbon coating on the BGO disk. This work was supported by the Grant-in-Aid for Specially Promoted Research 24000008 of Japanese Ministry of Education, Culture, Sports, Science and Technology (MEXT), Special Research Projects for Basic Science of RIKEN, European Research Council under European Union's Seventh Framework Programme (FP7/2007-2013)/ERC Grant Agreement (291242) and the Austrian Ministry of Science and Research, Austrian Science Fund (FWF): W1252-N27.

References

[1] N. Kuroda, et al., A source of antihydrogen for in-flight hyperfine spectroscopy, Nature Commun. 5 (2014) 3089.
[2] A. Mohri, Y. Yamazaki, A possible new scheme to synthesize antihydrogen and to prepare a polarized antihydrogen beam, Europhys. Lett. 63 (2003) 207.
[3] Y. Nagata, Y. Yamazaki, A novel property of anti-Helmholz coils for in-coil syntheses of a ntihydrogen atoms: formation of a focused spin-polarized beam, New J. Phys. 16 (2014) 083026.
[4] Y. Nagata, et al., The development of the superconducting double cusp magnet for intense antihydrogen beams, J. Phys. Conf. Ser. 635 (2015) 022062.
[5] M. Diermaier, et al., In-beam measurement of the hydrogen hyperfine splitting and prospects for antihydrogen spectroscopy, Nature Commun. 8 (2017) 15749.
[6] ASACUSA proposal addendum, CERN/SPSC 2005-002, SPSC P-307 Add 1, 2005.
[7] E. Widmann, et al., Measurement of the hyperfine structure of antihydrogen in a beam, Hyperfine Interact. 215 (2013) 1.
[8] N. Kuroda, et al., Antihydrogen synthesis in a double-cusp trap, JPS Conf. Proc. 18 (2017) 011009.
[9] M. Tajima, et al., Manipulation and transport of antiprotons for an efficient production of antihydrogen atoms, JPS Conf. Proc. 18 (2017) 011008.
[10] C. Malbrunot, et al., The ASACUSA antihydrogen and hydrogen program : results and prospects, Philos. Trans. R. Soc. Lond. Ser. A Math. Phys. Eng. Sci. 376 (2018) 20170273.
[11] Y. Nagata, et al., Direct detection of antihydrogen atoms using a BGO crystal, Nucl. Instrum. Methods Phys. Res. A 840 (2016) 153.
[12] C. Sauerzopf, et al., Annihilation detector for an in-beam spectroscopy apparatus to measure the ground state hyperfine splitting of antihydrogen, Nucl. Instrum. Methods Phys. Res. A 845 (2016) 579.
[13] Y. Nagata, et al., The development of the antihydrogen beam detector: toward the three dimensional tracking with a BGO crystal and a hodoscope, JPS Conf. Proc. 18 (2017) 011038.
[14] C. Sauerzopf, et al., Intelligent front-end electronics for silicon photodetectors (IFES), Nucl. Instrum. Methods Phys. Res. A 819 (2016) 163.
[15] C. Sauerzopf, et al., Towards measuring the ground state hyperfine splitting of antihydrogen - a progress report, Hyperfine Interact. 237 (2016) 103.
[16] S.Agostinelli, et al., Geant4.a simulation toolkit, Nucl. Instrum. Methods Phys. Res. A 506 (3) (2003) 250.
[17] C. Hagmann, et al., IEEE Nucl. Sci. Symp. Conf. Record, vol. 2, 2007, p. 1143.
[18] W.R. Leo, Techniques for Nuclear and Particle Physics Experiments, Springer-Verlag, 1993.
[19] K.A. Olive, et al. (Particle Data Group), Chin. Phys. C 38 (2014) 090001.
[20] S. Aghion, et al., Measurement of antiproton annihilation on Cu, Ag and Au with emulsion films, J. Instrum. 12 (2017) P04021.
[21] M. Hori, et al., Analog Cherenkov detectors used in laser spectroscopy experiments on antiprotonic helium, Nucl. Instrum. Methods Phys. Res. A 496 (2003) 102.